RSC Advances

PAPER

View Article Online
View Journal | View Issue

Cite this: *RSC Adv.*, 2016, **6**, 108726

Ni(II) complex with bishydrazone ligand: synthesis, characterization, DNA binding studies and pro-apoptotic and pro-differentiation induction in human cancerous cell lines†

Nenad R. Filipović,*[a] Snežana Bjelogrlić,[b] Tamara R. Todorović,[c] Vladimir A. Blagojević,[d] Christian D. Muller,[e] Aleksandar Marinković,[f] Miroslava Vujčić,[g] Barbara Janović,[g] Aleksandar S. Malešević,[c] Nebojša Begović,[h] Milan Senćanski[i] and Dragica M. Minić[j]

Received 2nd October 2016
Accepted 4th November 2016

DOI: 10.1039/c6ra24604d

www.rsc.org/advances

A new Ni(II) complex, [Ni(L)(H_2O)] (**1**), with diethyl 3,3′-(2,2′-(1,1′-(pyridine-2,6-diyl)bis(ethan-1-yl-1-ylidene))bis(hydrazin-1-yl-2-ylidene))bis(3-oxopropanoate) ligand (H_2L) was synthesized as a potential chemotherapeutic agent. Polidentate ligand was coordinated to Ni(II) *NNN*-tridentately, in dianionic form, while monodentate water coordination completed square-planar geometry around metal. Structure in the solution was determined by NMR spectroscopy and the same coordination mode was observed in the solid state using IR spectroscopy and further verified by DFT calculations and electrochemical studies. Thermal stability of **1** was determined in both air and nitrogen atmosphere. Anticancer activity of **1** was investigated on acute monocytic leukemia (THP-1) and pancreatic adenocarcinoma (AsPC-1) cell lines. On THP-1 cells **1** induced powerful apoptotic response ($ED_{50} = 10 \pm 3$ μM), which was revealed to be only partially caspase-dependent, with activation of caspase-8 as the dominant course. This suggested that experimentally validated covalent binding of **1** to DNA is not the only mechanism responsible for programmed cell death. This was supported with experiments on AsPC-1 cells. Although treatment of those cells with **1** resulted in poor apoptotic response, cell cycle changes showed concentration-dependent shifts indicating a dual mechanism of activity. This study also reviews the results of preliminary biological screening, which demonstrates that **1** displays a unique pattern of anticancer activity with at least two mechanisms involved.

Introduction

Ni(II) complexes with hydrazone ligands have been a focus of intense research, due to their application in hydrogen production[1] and catalysis,[2,3] as well as their magnetic properties,[2,4] application for data storage[5,6] and as flame retardants.[7] Nickel is an essential micronutrient in many microorganisms, and enzymes involved in several critical metabolic processes contain nickel as a co-factor,[8] making nickel complexes a subject of many biological studies.[9,10] On the other hand, hydrazone ligands create the local environment similar to that in the biological systems – coordination through O and N atoms to a metal center, and their –NH and –CO groups can participate in hydrogen bonding and represent potential deprotonation-protonation sites.[11] Inorganic medicinal chemistry is a growing field, investigating use of metal complexes in drug discovery. Complex formation results in species with novel structural scaffolds and electronic properties that are not accessible through organic compounds. The important property of these metal complexes is the ability to undergo ligand

[a]*Faculty of Agriculture, University of Belgrade, Nemanjina 6, 11000 Belgrade, Serbia. E-mail: nenadf.chem@gmail.com*
[b]*National Cancer Research Center of Serbia, Pasterova 14, 11000 Belgrade, Serbia*
[c]*Faculty of Chemistry, University of Belgrade, Studentski trg 12-16, 11000 Belgrade, Serbia*
[d]*Institute of Technical Sciences SASA, Knez Mihailova, 35/IV, 11000 Belgrade, Serbia*
[e]*Institut Pluridisciplinaire Hubert Curien, UMR 7178 CNRS Université de Strasbourg, 67401 Illkirch, France*
[f]*Faculty of Technology and Metallurgy, University of Belgrade, Karnegijeva 4, 11000 Belgrade, Serbia*
[g]*Institute of Chemistry, Technology and Metallurgy, University of Belgrade, Njegoševa 12, 11000 Belgrade, Serbia*
[h]*Institute of General and Physical Chemistry, Studentski trg 12, 11000 Belgrade, Serbia*
[i]*Center for Multidisciplinary Research, Institute of Nuclear Sciences "Vinča", University of Belgrade, 11000 Belgrade, Serbia*
[j]*Faculty of Physical Chemistry, University of Belgrade, Studentski trg 12-16, 11000 Belgrade, Serbia*

† Electronic supplementary information (ESI) available: Mass spectrum (Fig. S1); NMR spectra (Fig. S2–S8); experimental and calculated ^{1}H and ^{13}C NMR chemical shifts (Tables S1 and S2); cyclic voltammogram (Fig. S9); concentration-response curve and ED_{50} value (Fig. S10). See DOI: 10.1039/c6ra24604d

exchange reaction with biomolecules, making them DNA, protein and enzyme targeting molecules, which display activity against diseases such as cancer, diabetes, anti-inflammatory disorders, neurological disorder and infectious diseases. The structure of these complexes depends on the nature of the organic ligands and the oxidation state of the metal center.[12–14]

Hydrazone complexes of Ni exhibit a wide spectrum of biological activity,[11] and a number of these complexes have shown higher anti-cancer activity than the drugs approved for treatment of certain types of cancer.[15–29] Ni(II) ion has d^8 electronic configuration, same as Pt(II) – the metal ion in, so far, all of the approved anti-cancer treatment drugs: cisplatin (CDDP), carboplatin, oxaliplatin, nedaplatin, and lobaplatin.[30] Unlike Pt(II), which only exhibits square-planar geometry (coordination number four), Ni(II) often exhibits higher coordination numbers, offering greater variation in geometry.

A choice of ligand can dictate square-planar geometry of Ni(II) hydrazone complexes, like dihydrazone ligands obtained from 2,6-diacetylpyridine (dap) and various hydrazone derivatives which coordinate asymmetrically to Ni(II) building square-planar complexes.[31–36] *N*-Acylhydrazone (NAH) moiety has been characterized as a privileged structure in anticancer research.[37] Molecules containing NAH moiety can be prepared by condensation of carbonyl compounds with malonic acid dyhidrazide (dhm), resulting in dyhidrazones and their complexes, which show promising anticancer activity.[38–42] It is well known that condensation reaction between dap and dhm yields macrocyclic dyhidrazone, which forms an octahedral complex with Ni(II). In order to prevent the formation of macrocyclic dyhidrazone based on dap, we introduced a new *N*-acylhydrazide, ethyl 3-hydrazino-3-oxopropionate (emh), in anticancer research by replacing one of hydrazide group in dhm with ester group. Here we present the synthesis of a new square-planar Ni(II) complex [Ni(L)(H_2O)] (**1**) with the *in situ* obtained diethyl 3,3′-(2,2′-(1,1′-(pyridine-2,6-diyl)bis(ethan-1-yl-1-ylidene))bis-(hydrazin-1-yl-2-ylidene))bis(3-oxopropanoate) ligand (H_2L), which is a product of condensation of dap with emh and its characterization in both the solid state and the solution. Thermal stability of this complex was investigated and its anticancer activity was compared to CDDP, with a study of its interaction with DNA in order to understand its reaction mechanism in biological systems. To the best of our knowledge, this is the first anti-cancer study of a bishydrazone square-planar complex of Ni(II) containing dap.

Experimental

General remarks

Hydrazine hydrate (55%) and dap (99%) were obtained from Acros Organics, while diethyl malonate (98%) was obtained from Merck. Solvents (ethanol 96% and diethyl ether) were used without further purification. Elemental analyses (C, H, N) were performed by the standard micro-methods using the ELEMENTAR Vario ELIII C.H.N.S=O analyzer. Infra-red (IR) spectra were recorded on a Thermo Scientific Nicolet 6700 FT-IR spectrophotometer by the Attenuated Total Reflection (ATR) technique in the region 4000–400 cm^{-1}. Abbreviations used for the IR spectra interpretation are: s (strong) and m (medium strong). Molar conductivity measurements were performed at ambient temperature on the CrisonMultimeter MM41 in methanol ($c = 1 \times 10^{-3}$ mol dm^{-3}). The ligand coordination mode in the complex was determined by NMR spectroscopy results: 1D (^1H and ^{13}C), 2D COSY, 2D NOESY and 2D ROESY, as well as 2D heteronuclear correlation HSQC and HMBC. The NMR spectra were obtained on BrukerAvance 500 equipped with broad-band direct probe. All spectra were measured at 298 K in $CDCl_3$. Chemical shifts are given on δ scale relative to tetramethylsilane as an internal standard for ^1H and ^{13}C. Abbreviations used for ^1H NMR spectrum: s, singlet; d, doublet; t, triplet; q, quartet. Electron spray ionization mass spectrum (ESI-MS) was recorded on LTQ Orbitrap XL spectrometer in a positive ion mode. UV-Vis spectrum was recorded on Shimadzu PharmaSpec UV-1700 spectrophotometer. Melting points were recorded on Stuart SMP10 without correction.

Synthesis of emh

Emh was synthesized according to the previously published method.[34] Product was recrystallized from ethanol. Melting point of the product (69–72 °C) is in good agreement to data previously published (68–69 °C).[43]

Synthesis of 1

Into the solution of dap (0.3 g, 1.839×10^{-3} mol) and emh (0.54 g, 3.675×10^{-3} mol) in ethanol (60 mL), $Ni(CH_3COO)_2 \cdot 4H_2O$ (0.45 g, 1.839×10^{-3} mol) was added. The reaction mixture was refluxed for 45 min and cooled to ambient temperature. Three days later red precipitate was filtered off, washed with ethanol and diethyl ether and dried in a desiccator. Yield: 0.27 g (29.7%). Mp = 180–182 °C. Anal. calcd for $C_{19}H_{25}N_5NiO_7$ (%): C, 46.18; H, 5.10; N, 14.17%. Found: C, 46.18; H, 4.92; N, 14.34%. Λ_M (1×10^{-3} M, MeOH): 1.20 Ω^{-1} cm^2 mol^{-1}. IR (ATR, cm^{-1}): 3559 (s) ν(O–H); 1733 and 1673 (s) ν(C=O); 1635 (m) ν(C=N). ^1H NMR (500.26 MHz, $CDCl_3$), δ: 8.44 (t, 1H, H–C3, $^3J_{3,2} = {}^3J_{3,2} = 7.9$ Hz), 7.97 (d, 1H, H–C2, $^3J_{2,3} = 7.9$ Hz), 7.83 (d, 1H, H–C4, $^3J_{4,3} = 7.9$ Hz), 4.25 (q, 2H, H–C11, $^3J_{11,12} = 7.1$ Hz), 4.17 (q, 2H, H–C18, $^3J_{18,19} = 7.1$ Hz), 3.72 (s, 2H, H–C16), 3.44 (s, 2H, H–C9), 2.43 (s, 3H, H–C14), 2.29 (s, 3H, H–C7), 2.11 (s, 2H, H_2O), 1.33 (t, 3H, H–C12, $^3J_{11,12} = 7.1$ Hz), 1.29 (t, H–C19, 3H, $^3J_{18,19} = 7.1$ Hz); ^{13}C NMR (125.80 MHz, $CDCl_3$), δ: 182.10 (C8), 178.04 (C15), 169.76 (C17), 168.60 (C10), 156.23 (C5), 153.08 (C6), 141.60 (C3), 137.80 (C1), 131.57 (C13), 124.64 (C2), 123.19 (C4), 61.29 (C11), 60.58 (C18), 45.48 (C16), 37.96 (C9), 20.98 (C14), 14.18 (C12), 14.11 (C19), 12.06 (C7). ESI-MS: $[M - H_2O + H^+]^+$ ($C_{19}H_{24}N_5NiO_6$) calcd. m/z 476.1080, found 476.1069.

Thermal analysis

Non-isothermal differential scanning calorimetry (DSC) measurements in nitrogen were carried out using DSC Q1000 (TA Instruments) with typical sample weight of 2.0 ± 0.2 mg, in nitrogen atmosphere with gas flow rate of 50 mL min^{-1}, in 25–300 °C temperature region. Non-isothermal thermal gravimetric analysis (TG) in air was conducted using PerkinElmer

PyrisDiamond TG/DTA, which provides simultaneous TG, DTG, DTA and DSC data. The measurements were conducted with air flow rate of 150 mL min^{-1}, in 25–600 °C range at different heating rates. TG measurement in nitrogen was conducted using the same instrument in 25–1000 °C range, with nitrogen flow rate of 150 mL min^{-1}. Calibration of thermal analysis instruments was conducted for each heating rate separately. Analysis of thermal data was conducted using ThermV software package 0.2.[44]

Cyclic voltammetry (CV)

CV measurements were performed using an electrochemical system CH Instruments (USA). The electrochemical cell (10 mL) consisted of a three-electrode system: glassy carbon electrode (inner diameter of 3 mm; CHI 104), an Ag/AgCl (saturated KCl) reference electrode and Pt counter electrode. The potential was swept over the range from −2.5 to +1.5 V (*vs.* Ag/AgCl) at scan rate of 100 mV s^{-1}. Measurements were performed at room temperature with deaeration of the solutions by passing a stream of nitrogen through the solution for 5 min and maintaining a blanket atmosphere of nitrogen over the solution during the measurement. The potentials were measured, and are quoted relative to Ag/AgCl reference electrode.

DFT calculations

DFT calculations on molecular systems were performed using Gaussian 09 rev. D[45] and ORCA v3.0.2 (ref. 46) program packages. Gaussian package was used for structure optimization and frequency analysis. All structures where fully optimized using C-PCM solvation method with Klamt radii.[47] In calculations we used the hybrid HF/DFT method with a combination of the three-parameter Becke[48] exchange functional and the Lee–Yang–Parr (B3LYP)[49] non-local correlation functional and Beck's exchange functional combined with Perdew's[50] (BP86) non-local correlation functional. ORCA package was employed for constraint relaxed surface scan at same theoretical level as in Gaussian 09, using COSMO solvation model. In addition, for calculations with ORCA package, exchange and correlation functional of Perdew, Burke and Ernzerhof (PBE)[51,52] were used. For the metal center LANL2DZ basis set was used in Gaussian and TZVP in ORCA, while 6-31G(d,p) basis set was used for the rest of the atoms in both Gaussian and ORCA calculations. IR spectrum was calculated using the molecular system in water solvent, while TD-DFT calculation of this system was performed, calculating 50 states, to obtain the calculated UV-Vis spectrum. Elucidation of vibrational spectra of calculated structures was conducted using potential energy distribution (PED) analysis implemented in VEDA package.[53]

Interactions with DNA

Fluorescence displacement experiments. A calf thymus DNA(CT-DNA; lyophilized, highly polymerized, Serva, Heidelberg) was dissolved in Tris buffer (10 mM Tris–HCl pH 7.9) overnight at 4 °C. This stock solution was stored at 4 °C and was stable for several days. A solution of CT-DNA in water gave a ratio of UV absorbance at 260 and 280 nm, A_{260}/A_{280} of 1.89–2.01, indicating that DNA was sufficiently free of protein. The concentration of DNA (2.86 mg mL^{-1}) was determined from the UV absorbance at 260 nm using the extinction coefficient $\varepsilon_{260} = 6600\ M^{-1}\ cm^{-1}$.[54] UV-Vis spectrum was recorded on a UV-1800 Shimadzu UV/Visible spectrometer operating from 200 to 800 nm in 1.0 cm quartz cells.

The competitive interactions of **1** and the fluorescence probes, Hoechst 33258 (H) and ethidium bromide (EB) with CT-DNA have been studied by measuring the change of fluorescence intensity of the probe-DNA solution after addition of **1**. Reaction mixtures containing 100 μM of CT-DNA (calculated per phosphate) in 1 mL of 40 mM bicarbonate solution (pH 8.4) were pretreated with 1 μL of the probe solution (25 μM of EB and 28 μM of H at final concentrations) for 20 min and the mixture was analyzed by fluorescence measurement. Then the gradually increasing concentrations of the complex (final concentrations 2, 4, 6, 8 10, 12, 16, and 20 μM) successively added and the change in the fluorescence intensity was measured using a Thermo Scientific Lumina Fluorescence spectrometer (Finland) equipped with a 150 W Xenon lamp. The slits on the excitation and emission beams were fixed at 10 nm. All measurements were performed by excitation at 500 nm in the range 520–700 nm for EB and by excitation at 350 nm in the range 390–600 nm for H. The control was the probe–CT-DNA solution. **1** did not have fluorescence under applied conditions.

Thermal denaturation. Thermal denaturation experiments were carried out by monitoring the absorption intensity of the CT-DNA at 260 nm varying the temperature from 60 to 100 °C in the absence and presence of the complex at ratio 2 : 1 with ramp rate of 1 °C min^{-1} in 10 mM phosphate buffer (pH 7.0) in CINTRA 40 UV-Vis spectrometer equipped with a Peltier element.

Electrophoretic mobility shift assay. The plasmid pUC19 (2686 bp, Sigma-Aldrich, USA) was prepared by its transformation in chemically competent cells *Escherichia coli* strain XL1 blue. Amplification of the clone was done according to the protocol for growing *E. coli* culture overnight in LB medium at 37 °C (ref. 55) and purification was performed using Qiagen Plasmid plus Maxi kit. Finally, DNA was eluted in 10 mM Tris–HCl buffer and stored at −20 °C. The concentration of plasmid DNA (512 ng μL^{-1}) was determined by measuring the absorbance of the DNA-containing solution at 260 nm. One optical unit corresponds to 50 μg mL^{-1} of double stranded DNA.

Supercoiled pUC19 DNA (512 ng) was subjected to different concentrations of **1** was investigated and incubated in a 20 μL reaction mixture in 40 mM bicarbonate buffer (pH 8.4) at 37 °C, for 90 min. The reaction mixtures were vortexed from time to time. The reaction was terminated by short centrifugation at 6708*g* and the addition of 5 μL of loading buffer [0.25% bromophenol blue, 0.25% xylene cyanol FF and 30% glycerol in TAE buffer, pH 8.24 (40 mM Tris–acetate, 1 mM EDTA)].

The samples were subjected to electrophoresis on 1% agarose gel (Amersham Pharmacia-Biotech, Inc) prepared in TAE buffer (pH 8.24). The electrophoresis was performed at a constant voltage (80 V) until bromophenol blue had passed through 75% of the gel. A Submarine Mini-gel Electrophoresis Unit (Hoeffer HE 33) with an EPS 300 power supply was used.

After electrophoresis, the gel was stained for 30 min by soaking it in an aqueous EB solution (0.5 μg mL^{-1}). The stained gel was illuminated under a UV transilluminator Vilber-Lourmat (France) at 312 nm and photographed with a Nikon Coolpix P340 Digital Camera through filter DEEP YELLOW 15 (TIFFEN, USA).

Cell cultures. Acute monocytic leukemia (THP-1, ATCC® TIB-202) and pancreatic adenocarcinoma (AsPC-1, ATCC® CRL-1682) cell lines were maintained in RPMI-1640 (Life Technologies, 11875-093) and DMEM high glucose (Sigma-Aldrich, D5796) cell culture media, respectively. Both media were supplemented with 10% (v/v) fetal bovine serum (FBS, Gibco, Cat. no. 16000-036) and 1% (v/v) penicillin–streptomycin (10 000 units per mL and 10 000 μg mL^{-1}, Gibco, Cat. # 15140-130). Cells were kept at 37 °C in atmosphere containing 5% (v/v) CO_2 during their exponential growth and during the course of experimental treatments.

Investigated compound was initially dissolved in dimethyl sulfoxide (DMSO) to the stock concentration of 20 mM. Further dilutions to the experimental concentrations applied on the cells have been done with RPMI-1640 or DMEM media immediately before each experiment, so that the highest final DMSO concentration never exceeded 0.5% (v/v).

Determination of pro-apoptotic activity. THP-1 and AsPC-1 cells were seeded in 96 flat bottom well plates (Corning® Costar®, Cat. no. CLS3596) in a volume 0.1 mL, at a density of 10 000 cells per well. Since the THP-1 cells grow in suspension, experimental treatments started within 2 h after cells seeding, while plates with adherent AsPC-1 cells were left overnight to settle. Investigated compound was added in a range of six rising concentrations. As controls, non-treated cells, cells treated with 0.5% DMSO, and cells treated with Celestrol (Enzo Life Sciences, Cat. no. ALX-350-332-M025) at 50 μM concentration were present in each 96-well plate.

After 24 h of incubation, THP-1 cells were centrifuged on 450*g* for 10 min, supernatants were discarded, and 0.1 mL of phosphate buffer saline (PBS) was added to each well. Plates were places on plate shaker for 3 min, afterwards Annexin V-FITC (ImmunoTools, Cat. no. 31490013) and propidium iodide (PI, MiltenylBiotec, Cat. no. 130-093-233) were added in a volume of 3 μL per well, respectively, and incubated for 15 min in the dark prior to cytometry. Post incubation manipulation with AsPC-1 cells included transfer of supernatant medium with non-adherent cells into another plate. Fresh PBS was added to remaining adherent cells afterwards the plates were centrifuged at 450*g* for 10 min. Supernatant was discarded and 200 μL of trypsin–EDTA (BioWest, Nuaille, France, Cat. No L0930-100) was added to each well. Cells were detached in about 15 min of incubation at 37 °C, afterwards another spinning cycle with supernatant elimination were performed. Finally, previously removed supernatant with non-adherent cells were added to trypsinized cells and stained with Annexin V-FITC and PI in a volumes of 3 μL. Plate analysis were performed on Guava® easyCyte 12HT Benchtop flow microcapillary cytometerusing InCyte® software package (EMD Millipore, Cat. no. 0500-4120). Cells were classified according to Annexin V and PI labeling on viable (non-stained cells), pre-apoptotic cells (stained with Annexin V only), cells in late phases of apoptosis (double stained cells), and necrotic cells (stained with PI only).

Calculation of ED_{50} concentration. Percent of Annexin V labeled cells for each concentration of investigated compound were summarized and maximum apoptotic response was normalized to 100%. Percent of apoptosis read out for other concentrations were calculated as a proportion of the highest response. Such scaled apoptotic outcomes were plotted against concentrations and ED_{50} concentration was calculated using asymmetric sigmoidal curve five-parameter logistic equation (GraphPad Prism 6 software). Determined ED_{50} concentration was applied in further steps of this investigation.

Cell cycle analysis. Cell cycle was evaluated either after cells were treated with ED_{50} concentration of the investigated compound for different time periods (6, 9, 12 and 24 h), or on cells already stained by Annexin V/PI readout as described previously.[56] In both cases, treated cells were fixed in ethanol overnight at 4 °C and then labeled by the FxCycle™ PI/RNAse Staining solution (Molecular Probes, Cat. no. F10797). Analyses were all performed on Guava® easyCyte 12HT Benchtop Flow microcapillary cytometer.

Inhibition of caspase activity. Cells were treated with investigated compound at ED_{50} concentration for 6 h with or without pan-caspase inhibitor *N*-benzyloxycarbonyl-Val-Ala-Asp (O–Me) fluoromethyl ketone (Z-VAD-fmk, Promega, Cat. no. G7232). As controls, non-treated cells, cells treated with Z-VAD-fmk only, and cells treated with ED_{50} concentration only were used. After incubation period was ended, treated cells were carried out for Annexin V/PI staining as described above, and analyzed on Guava® easyCyte 12HT cytometer. The percent of apoptosis inhibited by Z-VAD-fmk co-treatment was determined by following formula:

$$\%\ \text{of inhibition} = [1 - (\%\ \text{of apoptosis or necrosis in A}/\%\ \text{of apoptosis or necrosis in B})] \times 100\% \quad (1)$$

where A is the sample treated with both ED_{50} concentration and Z-VAD-fmk, and B the corresponding sample treated with ED_{50} concentration only.

Evaluation of caspase-8 and -9 activities. Cells were treated with investigated compound at ED_{50} concentration for 6 h afterwards activity of caspase-8 and -9 were assayed by means of Guava Caspase 9 SR and Caspase 8 FAM kit (EMD Millipore, Cat. no. 4500-0640), following instructions of manufacturer. In acquired data cells were discriminated according to expression of green fluorescence (caspase-8), yellow fluorescence (caspase-9), or red fluorescence (7-AAD) as the following: live cells (not stained with either caspase nor 7-AAD); mid stage apoptotic cells (cells stained with either caspase-8 or -9, but negative to 7-AAD); late stage apoptotic cells (cells stained with either of caspase-8 or -9 and with 7-AAD); necrotic cells (cells not stained with neither caspase-8 nor -9, but positive for 7-AAD). Percentages of treated cells that express caspase activity were calculated relative to non-treated control computed separately for cells which expressed activated either caspase-8 or -9, and cells that showed activity of both caspases using formula:

Relative activity, % = [% of treated cells expressing caspase(s)/ % of non-treated cells expressing caspase(s)] × 100% (2)

Results and discussion

General

Red precipitate of Ni(II) complex was obtained by the template reaction of dap and emh with $Ni(CH_3COO)_2 \cdot 4H_2O$ in ethanol (1 : 2 : 1) (Scheme 1). The product was soluble in methanol, acetonitrile, chloroform, dimethyl formamide and DMSO, partially soluble in ethanol and insoluble in diethyl ether and water. Magnetic measurement indicated that the complex is diamagnetic, while the value of its molar conductivity in methanol is 1.20 Ω^{-1} cm^2 mol^{-1}, significantly less than for 1 : 1 electrolytes.[57] Elemental analysis showed that the complex consists of Ni(II) ion, dianionic ligand and one water molecule. Based on these results, the following general formula can be written [Ni(L)(H_2O)] mass spectrum of the complex recorded in acetonitrile shows the most intense peak at m/z = 476.1069, corresponding to the fragment $[NiL - H_2O + H^+]^+$, with the appropriate isotope pattern (Fig. S1, ESI†).

Structural and electrochemical studies

1D (^1H and ^{13}C) and 2D (COSY, NOESY, ^1H–^{13}C HSQC and ^1H–^{13}C HMBC) NMR spectra of **1** in $CDCl_3$ are shown in Fig. S2–S8 (ESI†), while the atom numbering scheme was given in Scheme 1. The number of signals observed in ^{13}C NMR spectrum of **1** (total of 19) indicate asymmetric coordination of L^{2-} to Ni(II), since 10 signals of carbon atoms are expected for symmetrical coordination of the ligand. In ^1H NMR spectrum of **1** 11 signals were detected. A signal at 2.11 ppm in ^1H NMR spectrum was assigned to the water molecule coordinated to the Ni(II) ion. This signal is significantly shifted downfield in comparison to the signal of non-coordinated water in $CDCl_3$ which appears at 1.56 ppm.[58] Similar situation, where respective solvents had similar polarity to the solvents used in our system, was observed in square-planar nickel(II) complex with contains diphosphane ligand and coordinated water molecules, where structure was solved with single crystal X-ray analysis.[59] NMR study in CD_2Cl_2 solution determined downfield shift of coordinated water (2.30 ppm) in comparison to non-coordinated water (1.52 ppm).[60] The difference in chemical shifts of 22.51 ppm between imine carbonyl atoms C6 (153.1) and C13 (131.6) indicated that imine nitrogen N2 is coordinated to Ni(II), since electron density of C=N bond is shifted towards Ni(II). Difference in chemical shifts of C8 and C15 atoms is not as large ($\Delta\delta$ = 4.06 ppm), indicating that oxygen atoms O2 and O3 do not participate in the coordination to the metal.

In the ^1H NMR spectrum, H–C16 was shifted downfield in comparison to its analogue H–C9, indicating coordination through N5. The coordination sphere of Ni(II) in this square-planar environment is completed by coordination of pyridine nitrogen which is corroborated by DFT calculations (*vide infra*). The coordination of pyridine nitrogen is likely to occur, since it results in formation of two stable chelate rings. Based on this information, the proposed structure of **1** is given in Scheme 1.

Proposed geometry around Ni(II) in **1** was further confirmed by theoretical DFT calculations. Independent of the starting geometry, the complex was always optimized to the slightly distorted square-planar geometry as shown in Fig. 1. In the optimized geometry, all three donor atoms from L^{2-}, nickel, and water oxygen atoms are in the same plane. Angles around Ni(II) are slightly distorted from ideal square-planar geometry due to steric hindrances in tridentate L^{2-} ligand (angle N1–Ni–

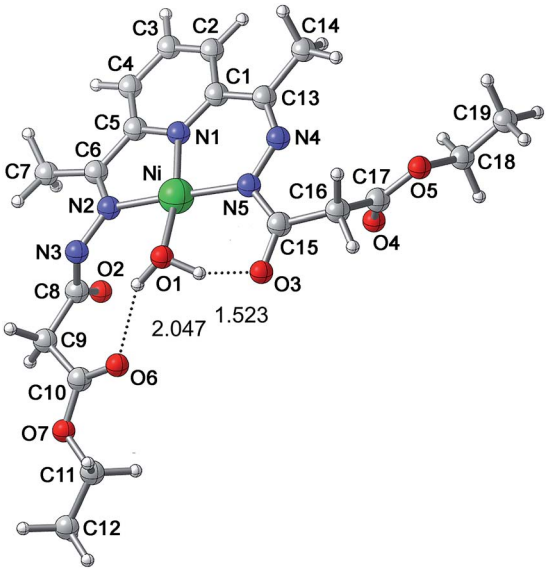

Fig. 1 The optimized structure of **1**.

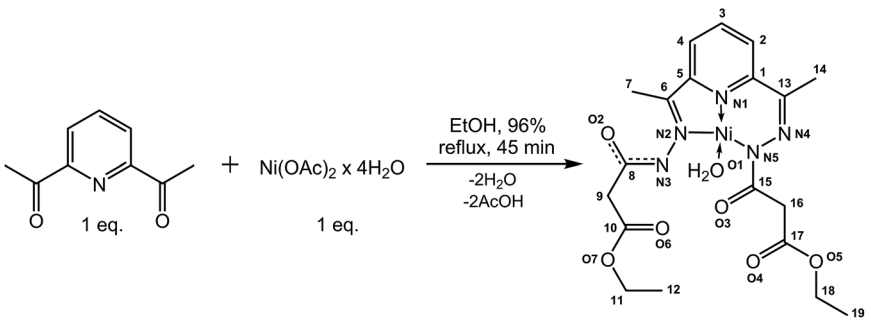

Scheme 1 Preparation of the complex [Ni(L)(H_2O)] (**1**).

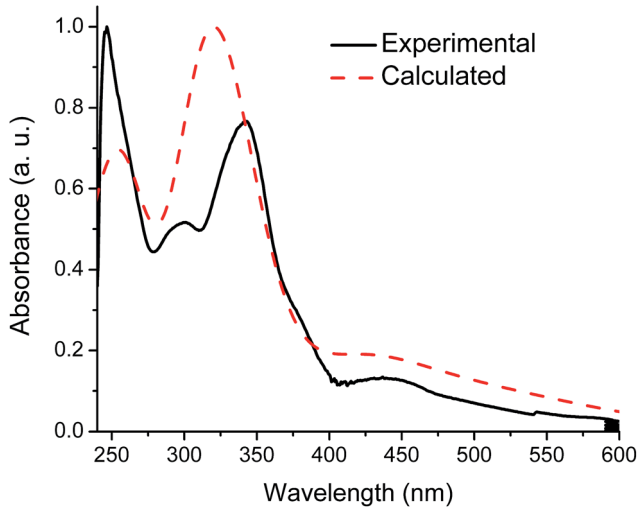

Fig. 2 Comparison of experimental and calculated UV-Vis spectra of **1**.

N2 = 84.4°; angle N5–Ni–N1 = 96.2°). Results of the calculated ^{1}H and ^{13}C NMR spectra of **1** (Tables S1 and S2, ESI†) show good agreement with experimental data, indicating that the actual geometry of **1** closely corresponds to the proposed one. The only significant deviation comes in the chemical shift of the water molecule proton, where one of the protons exhibits much higher chemical shift than observed in the experiment. This can be explained by the fact that the calculation was performed on a monomer system in a continuous dielectric, taking no account of intermolecular interactions. As a consequence, these two protons exhibit significantly different hydrogen bond lengths (Fig. 1), and the proton with shorter hydrogen bond exhibits higher chemical shift.

The experimental spectrum suggests that both water protons are equivalent, suggesting that the orientation of the molecule in the solution is most likely such that the hydrogen bonding to two water protons is achieved either through O6 and O4 oxygen and not O2 and O3, or through intermolecular hydrogen bonding, making hydrogen bonds longer. This suggests that the geometry is probably dictated by intermolecular interactions, where this orientation would make the entire molecule roughly planar in the coordination plane of the metal center, providing better geometry for interactions above and below this plane.

UV-Vis spectrum of **1** in MeOH contains four bands (Fig. 2): three of them (439.50, 341.75, 296.68 nm) are assigned to electronic transitions of square-planar Ni(II) complex, and the fourth (245.18 nm) is assigned to the charge transfer between the ligand and Ni(II) ion (Table 1). There is a good agreement between experimental and the normalized calculated UV-Vis spectrum (with $N = 100$ calculated transitions) of **1**, as shown in Fig. 2. Since the optimized structure of **1** exhibits square-planar coordination around the metal center, this represents another confirmation of the band assignment.

Electrochemical behavior of **1** was investigated using CV on a glassy carbon working electrode in the potential range from −2.50 to +1.50 V *vs.* Ag/AgCl electrode in DMSO using [*n*-Bu$_4$N]PF$_6$ as supporting electrolyte. Under these experimental conditions, **1** undergoes irreversible redox processes, giving two reduction peaks at −1.77 and −2.00 V, and one oxidation peak at +0.98 V (Fig. S9, ESI†) with the onset of oxidation and reduction at $E_{ox.onset}$ = +0.68 V and $E_{red.onset}$ = −1.58 V, respectively. From these values,[61] where ferrocene was used as an external standard, the energy gap ($E_g = E_{LUMO} - E_{HOMO}$) was calculated to be +2.26 eV, which is in good agreement with the value +2.33 eV, calculated from longest absorption wavelength λ_{onset} ($E_g = 1242/\lambda_{onset}$)[62] and the one obtained by DFT calculations +2.28 eV. However, DFT calculations gave the values of E_{HOMO} and E_{LUMO} as −5.78 eV and −3.44 eV, compared to the experimental values obtained from CV[63] of −4.93 and −2.67 eV, respectively. This significant difference between electrochemically obtained and calculated values is a consequence of high irreversibility of the observed electrochemical processes. This can be expected when irreversible electrochemical processes include, in addition to electronic transition, other limiting steps, which were not taken into account by the DFT model and UV spectra as well.

Table 1 Electronic spectral data for **1**

λ (nm)	A	ε (M^{-1} cm^{-1})	Assignation
439.50	0.1965	196 500	$^{1}A_{2g} \leftarrow {}^{1}A_{1g}$
341.75	1.0475	1 047 500	$^{1}B_{2g} \leftarrow {}^{1}A_{1g}$
296.68	0.7143	714 300	$^{1}E_{g} \leftarrow {}^{1}A_{1g}$
245.18	1.3807	1 380 700	L $\leftarrow$ Ni^{2+}

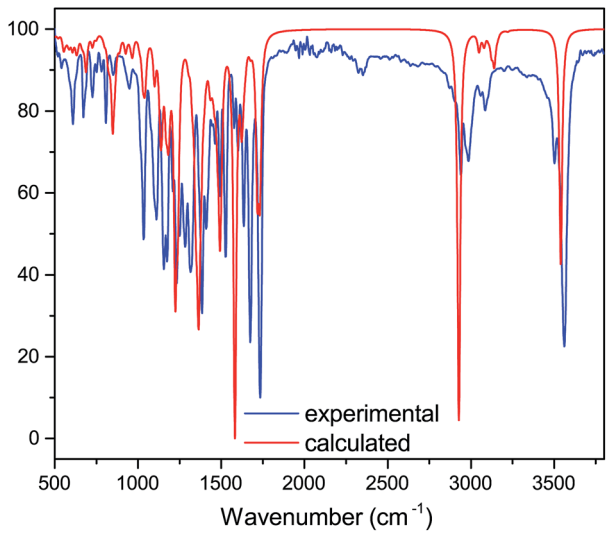

Fig. 3 Experimental and calculated IR spectra of **1**.

Experimental and calculated IR spectra for **1** are given in Fig. 3, with full assignment of the bands in Table 2. DFT calculations on a molecular system in a continuous water solvent resulted in good agreement between experimental and calculated IR spectra (Table 2), allowing assignment of the vibrations in the experimental IR spectrum using the results of the calculations.

Table 2 Selected experimental and calculated IR spectral data of **1**

Vibration	Type	Calculated ν (cm^{-1})	Experimental ν (cm^{-1})
O–H (water)	sym. stretch	3670, 2930	3559, 2939
C=O	sym. stretch	1729, 1718	1733.5
O–H (water)	sym. scissor	1690	1673
C=N	sym. stretch	1640, 1605	1634, 1600
C=N	sym. stretch	1590, 1560	1600, 1577
Ring vibration	sym. ring vibr.	1559	1525
C–H	sym. def.	1350, 1320	1363, 1313
C–O–C (ester)	asym. stretch	1229, 1208	1232, 1210
N–N	sym. stretch	1150	1156
O–H	Rocking	960	955
Ring vibration	asym. ringvibr.	860	854.6
O–H (water)	asym.	801	807
C–C	sym. stretch	722.5	728

Thermal analysis

Thermal stability of **1** was analyzed in both air and nitrogen atmosphere using TG and DSC. TG thermal degradation curves of **1** in air and nitrogen reveal a significant difference of degradation processes, following different reaction pathways in different atmospheres (Fig. 4). Overall, thermal degradation starts around 200 °C and the step-wise mass loss is continuous until the end of degradation. **1** exhibits considerably faster mass loss in air, which is consistent with thermally induced oxidation. The final mass residue is consistent with the formation of nickel oxide as the final product: NiO in air and NiO_2 or NiOOH in nitrogen.

DSC of **1** heated in air exhibits an endothermic peak around 180–190 °C and a much larger exothermic peak in the 350–450 °C temperature domain (Fig. S13†), both peaks corresponding complex processes involving multiple overlapping degradation steps. All peaks exhibit a shift to higher temperatures with increase in heating rate, indicating thermal activation of degradation processes.

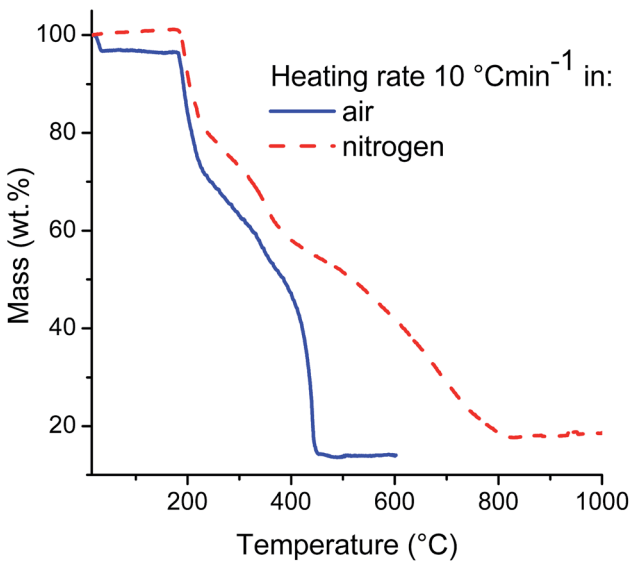

Fig. 4 TG curves recorded in nitrogen and air.

Table 3 Enthalpies of the endothermic peak 1 and the exothermic peak 2 recorded in air and nitrogen

Air		
Heating rate (°C min^{-1})	Enthalpy – peak 1 (kJ mol^{-1})	Enthalpy – peak 2 (kJ mol^{-1})
2	32.36	5736.76
4	42.55	6425.90
6	48.59	6665.53
10	80.95	7096.12

Nitrogen	
Heating rate (°C min^{-1})	Enthalpy – peak 1 (kJ mol^{-1})
4	12.56
5	20.91
10	29.69
15	33.30
20	36.1
35	33.57

When **1** was heated in nitrogen, it exhibited an endothermic process in 180–200 °C temperature domain, followed by a series of exothermic processes in 200–300 °C temperature domain (Fig. S14†). At lower heating rates, the endothermic process around 180 °C is not very well defined due to an overlap with an exothermic process, which follows. This complex region is followed by another exothermic peak around 220 °C. However, due to different thermal activation, the endothermic peak is well defined at higher heating rates (10–35 °C min^{-1}), with very little variation in overall enthalpy (Table 3).

Endothermic peak 1 exhibits relatively low values of enthalpy of the overall process (Table 3), both when recorded in nitrogen and in air, with higher values in air, and, at a heating rate of 10 °C min^{-1}, the changes in the observed values of enthalpy and peak shape (Fig. 5B) indicate increasing significance of diffusion of oxygen into the sample. Exothermic peak 2 exhibits very high values of enthalpy of the overall process, which is consistent with oxidation reaction at high temperature. The value of enthalpy and asymmetric peak shape indicate a very complex process involving a large number of atoms and breaking of several bonds.

The values of the overall activation energy for peaks in nitrogen and air were calculated using Kissinger and Ozawa methods.[64,65] The experimental peak 1 in nitrogen exhibits unusually high value of the overall activation energy, most likely due to the overlap with subsequent exothermic process (Table 4). The value of overall activation energy in air is much smaller, likely due to the presence of oxygen, which changes the reaction mechanism of thermal decomposition, ultimately leading to formation of different final products observed in TG curves in air and nitrogen. The overall activation energy of peak 2 in air is very small for a process occurring in 350–450 °C temperature domain and this, combined with a very high value of enthalpy,

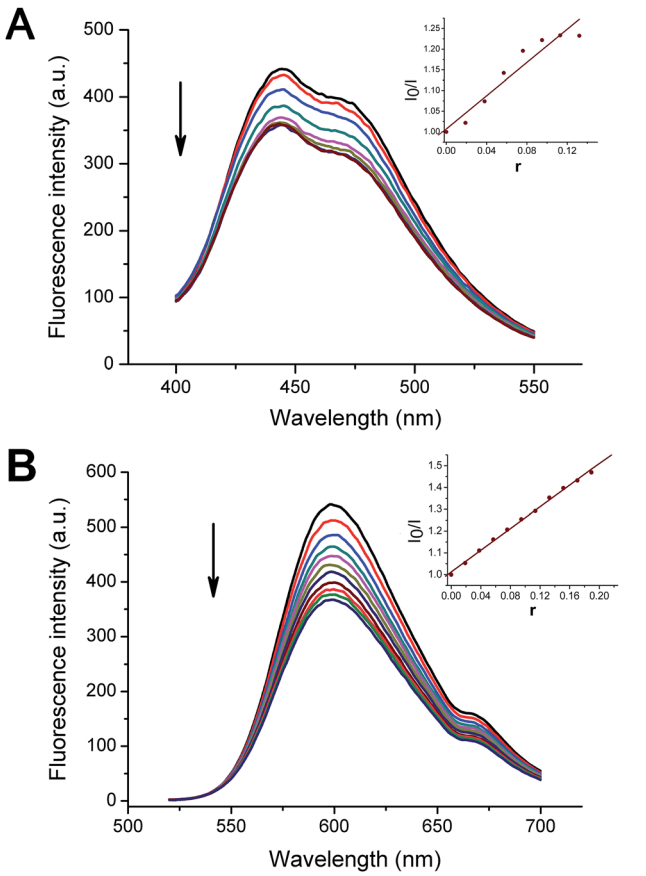

Fig. 5 Displacement of CT-DNA (100 μM, top line) bound H (25 μM), panel (A) and EB (28 μM) by **1**, panel (B), at increasing final concentrations (2, 4, 6, 8 10, 12, 16, and 20 μM, curves from top to bottom). The arrows show that fluorescence intensity decreased with increasing concentration of the complex. The insets demonstrate fluorescence quenching curves of H bound to CT-DNA at 444 nm and EB bound to CT-DNA at λ_{max} = 600 nm by **1**, panels (A) and (B), respectively; r = **1**/[CT-DNA].

Table 4 Overall activation energies for the endothermic peak 1 and the exothermic peak 2 recorded in air and nitrogen

Overall E_a (kJ mol^{-1})	Air peak 1	Air peak 2	N_2 peak 1
Kissinger method	290 ± 30	81 ± 5	1120 ± 50
Ozawa method	280 ± 30	87 ± 4	1080 ± 50

indicates that organic part of the molecule quickly oxidizes, most likely forming CO_2.

Interactions with DNA

Binding of small molecules with DNA and investigation of structural aspects of such bindings have turned out to be an emerging topic of interest from the perspective of medicinal chemistry, including cancer chemotherapy and development of new and more efficient therapeutic agents targeted to DNA.[45] Transition metal complexes can bind to DNA *via* both covalent and/or non-covalent interactions. In general, covalent interactions include coordination to DNA base, sugar and phosphate moieties, while non-covalent interactions include binding to minor groove, major groove, sugar-phosphate backbone, intercalation between the bases and binding to unique DNA structural motifs such as the three way junction, G-quadruplexes, cruciforms and hairpins.[66] In most cases metal complexes interact with DNA *via* minor groove, by intercalation and covalent binding.

Fluorescence quenching studies

Fluorescence spectroscopy is a widely used technique for study of DNA interaction with metal complexes. Fluorescence quenching of DNA-H dye adduct by the metal complex is an established method for determination of its propensity to bind to the DNA minor groove, and fluorescent displacement is widely used for investigation of intercalative properties of metal complexes. While H is only weakly fluorescent, its fluorescence yield increases significantly in the presence of DNA. In the case of minor groove binders, the reduction of fluorescence was found to be 55% or more.[67,68] However, the addition of **1** to CT-DNA caused only 19% reduction in the fluorescence intensity of H-CT-DNA system with maximal applied concentration of the complex (Fig. 5A), indicating that minor groove is not significant target for **1**.

Fluorescent displacement experiments were carried out with EB, well known dye which acts as a typical DNA intercalator.[69] Binding of EB to CT-DNA was followed by excitation at 500 nm with fluorescence maximum at 600 nm. The emission spectra of EB bound to CT-DNA in the absence and presence of **1** are given in Fig. 5B. It was observed that the increase in concentration of **1** causes a continuous decrease in the fluorescence intensity of the band at 600 nm of the EB-CT-DNA system, with the maximal decrease of 32%. EB fluorescence quenching by typical strong intercalators is almost complete,[70–72] while the values lower than 50% indicate mechanisms of fluorescence quenching different from intercalation.[73–75] Addition of **1** would quench the EB emission by either replacing the DNA-bound EB (if it binds to DNA more strongly than EB) or by accepting the excited state electron from EB. Since metal complexes with no extended planar rings are not expected to displace the intercalatively bound EB, small reduction of DNA-EB fluorescence intensity indicates that quenching occurs by photo electron-transfer mechanism.[76–78] Previous investigation on a series of Cu(II) complexes indicated that the ability of the complexes to quench the EB emission intensity by photo electron-transfer mechanism depends upon their reducibility: the complex with a more positive redox potential (−0.219 V) had the highest ability to quench the emission intensity of EB. Redox potential of **1** is even more positive, which indicates its capability to undergo photo electron-transfer mechanism.[79]

Thermal denaturation studies

Thermal behavior of DNA in the presence of metal complexes can give insight into DNA conformational changes with increase in temperature and the strength of DNA-complex interactions. The temperature at which half of the DNA sample is melted is known as the melting temperature (T_m), and it is strongly

related to the stability of the double-helical structure. An increase in melting temperature indicates that the metal complex has a stabilizing effect, while a decrease in T_m indicates destabilizing effect. High positive ΔT_m (3–8 °C) is characteristic for intercalation type of interaction,[72,80,81] while groove-binding interaction of small molecules with DNA leads to insignificant changes in T_m.[80,82–84] Negative values of ΔT_m indicate covalent binding.[85–87] In the case of **1**, the difference in melting temperatures ΔT_m ($\Delta T_m = T_m$ of free DNA – T_m of DNA-**1**) is −4.5 °C (Fig. 6), corroborating fluorescence quenching studies which show that **1** does not have a significant propensity to minor groove and does not intercalate. Negative value of ΔT_m indicates that this complex binds covalently to DNA.

Metal complexes which undergo covalent binding to DNA contain labile ligands which act as good leaving groups, such as Cl^- ion,[79] water[88,89] and solvent molecules.[90] Structure of 1 seems suitable for covalent bonding to DNA, since square-planar Ni complexes are capable to extend their coordination sphere by coordination of axial ligands, resulting in formation of octahedral complexes. Also, **1** contains a water molecule coordinated to Ni(II) ion which is a better leaving group than Cl^- ion. It is well known that CDDP, $[PtCl_2(NH_3)_2]$, the most famous covalent binding anticancer agent, needs to release the chloride before it binds to DNA. Within the cell, CDDP aquation of one or both chloride leaving groups occurs and resulting complexes $[Pt(H_2O)Cl(NH_3)_2]^+$ and $[Pt(H_2O)_2(NH_3)_2]^{2+}$ are the actual species which react with nucleophilic centers of biomolecules.[88]

Nitrogen atom N7 in guanine residues has a strong affinity for Ni(II):[91] it is 2.3 times more basic than corresponding nitrogen atom from adenine, which leads to 10 times larger binding affinity to metal ions.[92] Also, comparative binding experiments of Ni(II) complex containing solvent molecule bonded to metal centre to adenosine-5′-monophosphate and guanosine-5′-monophosphate by ESI-MS and NMR spectroscopy confirmed that binding tendency of nucleotides is higher for guanosine nucleotide.[90]

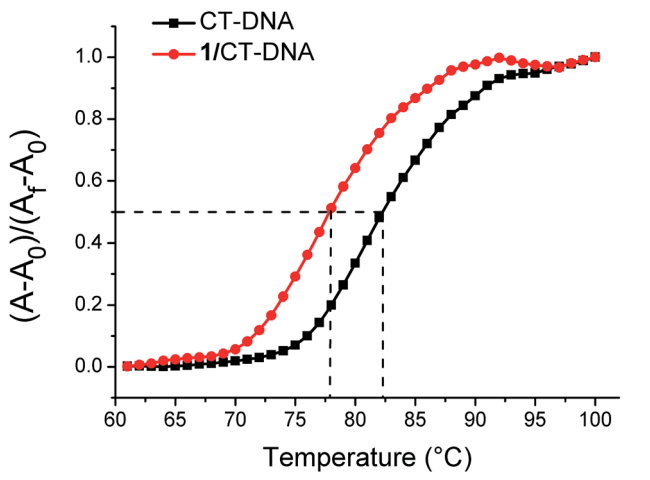

Fig. 6 Melting curves of CT-DNA (100 μM) in the absence and presence of Ni(II) complex (50 μM). A_0 is the initial absorbance intensity, A is the absorbance intensity corresponding to its temperature, A_f is the final absorbance intensity.

Gel electrophoretic studies

The interaction of metal complexes with double stranded closed circular plasmid DNA is usually monitored by agarose gel electrophoresis. This assay allows assessment of DNA strand cleavage by monitoring the conversion of untreated form (FI) plasmid DNA into the nicked form (FII) and linear form (FIII) in the case of DNA cleavage. Also, retardation of DNA indicates covalent binding of the investigated compounds. Upon addition of **1** to the plasmid, no strand scission was observed (Fig. 7, lanes 2 and 3) at concentrations up to 1.5 mM in comparison to the control (lane 1), indicating that DNA cleavage does not present a mode of action of this Ni(II) complex, *i.e.* the complex has no nuclease activity. Binding of the higher concentrations of the complex to the DNA causes the retardation of the plasmid forms in the gel. The electrophoretic pattern suggests that changes in conformations of the plasmid were caused by the binding of **1**, and retardation of the migration of DNA through the gel is observed for molecules which bind covalently to DNA.[93–95]

Evaluation of anticancer activity

Nickel hydrazone complexes have been extensively investigated for anticancer properties[15–29] but in general, the literature data deals with their activity described by IC_{50} concentrations with data obtained by mean of colorimetric assays. Such methodology provides only the information on how the applied compound reduces number of viable cells in the treated population with regard to non-treated control for a specific time of incubation, therefore, calculated IC_{50} value gives an indication on antiproliferative activity of investigated treatment, but not on how the treatment affected cell proliferation: by triggering apoptotic or necrotic cell death, due to prolongation of mitotic cycle with delayed population growth, or by induction of cell dormancy. In this study, the method employed for assessment of anticancer activity was Annexin V/PI double staining assay, which allows accurate qualitative and quantitative discrimination of cell death in terms of apoptosis and necrosis. It also enables us to observe if the compound concentration-dependently introduces treated cells from initial to advanced

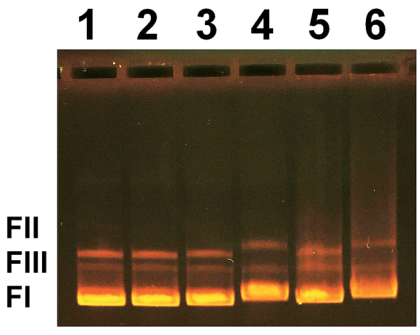

Fig. 7 Results of agarose gel electrophoresis of interaction of pUC19 with **1**. Lane 1 – control plasmid pUC19; lane 2, 3, 4, 5 and 6 – plasmid pUC19 with 1 mM, 1.5 mM, 2 mM, 2.5 mM and 3 mM of the complex, respectively.

phases of apoptotic death, which provides information on concentration-response relationship with preliminary insight into the span of therapeutic index. Besides these advantages, the method of our choice presents one limitation: it is not possible to directly compare activity of **1** to other nickel complexes that were evaluated with colorimetric assays.

Anticancer activity of **1** can be compared with activity of CDDP that is widely used for the treatment of broad-spectrum malignancies. Aside from the fact that both **1** and CDDP are metal complexes, those also share the same square-planar geometry with d^8 electronic configuration of divalent metal ions. The mechanism of CDDP anticancer activity has been studied for a long time, with new surprising discoveries even 30 years after the main breakthrough in its understanding. Treiber *et al.*[96] described the relation between DNA crosslinking by CDDP with high mobility group domain proteins and the consequently affected processes of transcription, replication and DNA repair, and their context of "transcription factor hijacking" is still considered the principal mechanism of CDDP activity. Nevertheless, it has been proven that CDDP also induces formation of reactive oxygen species,[97,98] chromosomal structural alterations,[99] down-regulation of microRNA

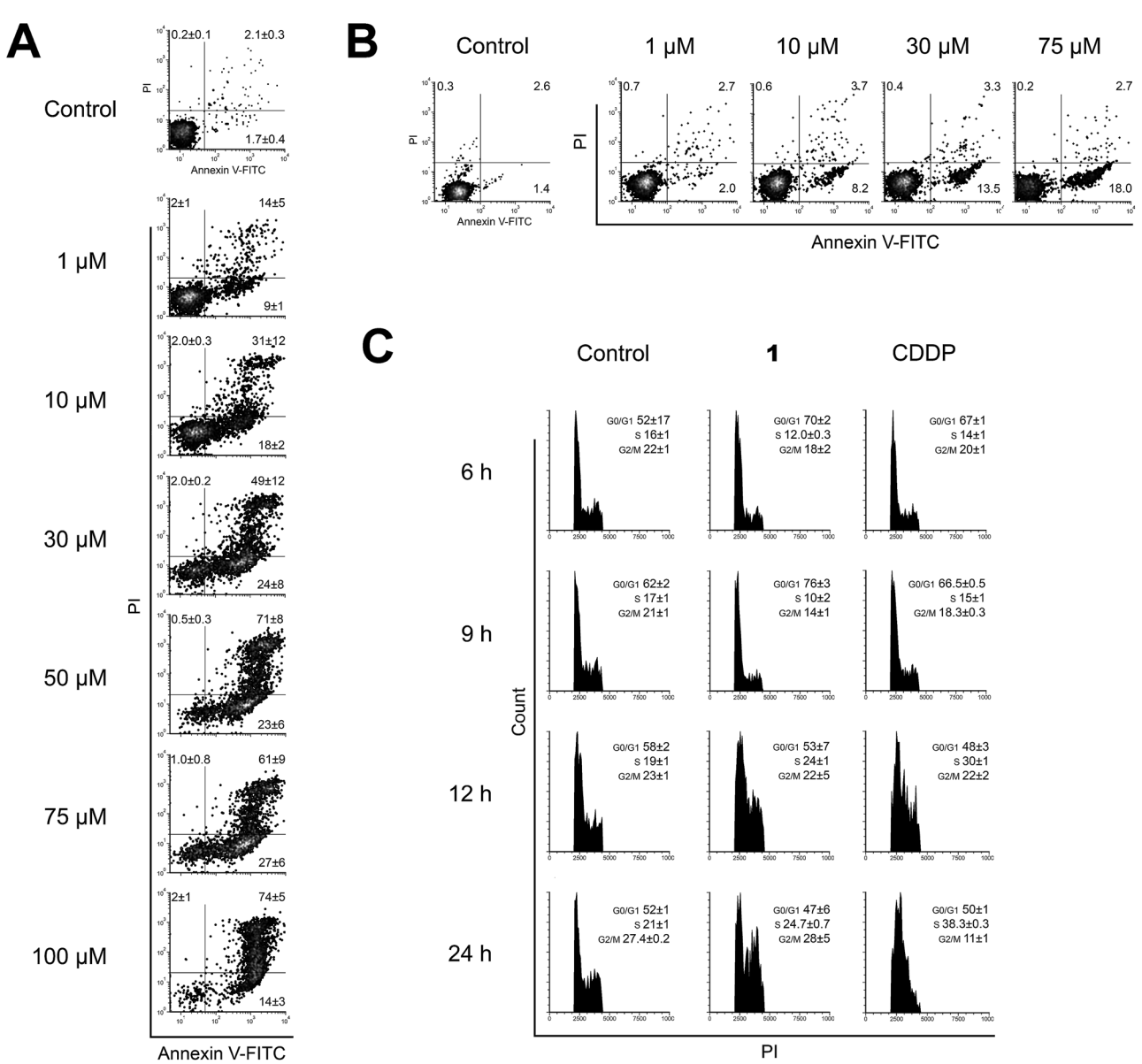

Fig. 8 Types of cell death and cell cycle changes in THP-1 cell line induced by the treatment with **1**. Results of Annexin V/PI double staining of THP-1 cells treated with **1** during 24 h (A), and during 6 h (B). In Annexin V/PI dot plots cells are discriminated as viable (non-stained cells, lower left quadrant), cells in early phase of apoptotic death (Annexin V single-stained cells, lower right quadrant), cells in advanced phases of apoptotic death (double-stained cells, upper right quadrant), and necrotic cells (PI single-stained cells, upper left quadrant). Cell cycle changes after different periods of incubation in cells treated with **1** and CDDP applied at their ED_{50} concentrations (C). Incidences of cells found at the G0/G1, S and G2/M phases were determined according to non-treated control population. Results of Annexin V/PI staining after 24 h treatment and cell cycle changes are expressed as the mean ± SD of two replicates from independent experiments.

expression,[100] and interferes with intracellular calcium signaling.[101–103] Some of these mechanisms are cell type-specific, some concentration- and/or time-dependent, however, they vindicate various cell cycle changes induced by CDDP treatment in different malignant cell lines. We have previously published results of CDDP activity on both THP-1 and AsPC-1 cell lines,[56] and herein we have investigated the activity of **1** in regards to CDDP.

Activity of **1** was firstly investigated on THP-1 cell line. Treatment involved 24 h incubation with **1** applied in a range of six concentrations (1–100 μM). For THP-1 cells **1** induced strong apoptotic response (Fig. 8A), with evidentially accelerating, concentration-dependent accumulation of cells from the early phase (Annexin V single-stained), to the advanced phases of apoptotic death (Annexin V/PI double-stained cells). At the same time, percentage of necrotic cells remained at the level of untreated control throughout the concentration range. Gradual evolution of apoptotic death was confirmed at 6 h incubation of THP-1 cells with **1**, when Annexin V single-stained cells were the dominant events in the samples subjected to concentrations which at 24 h treatment resulted in extensive percentage of late apoptosis (Fig. 8B). On the other hand, CDDP at 24 h caused concentration-dependent accumulation of THP-1 cells in the early phase of apoptotic death while just a small percent of them transitioned to the execution phase, even in the samples subjected to the highest applied concentration.[56] Concentration-response curve that describes activity of **1** is plotted with lower ED_{50} concentration (10 ± 3 μM, Fig. S10, ESI†) than CDDP (17.8 ± 0.2 μM).[56]

Although **1** and CDDP induce different apoptotic responses in THP-1 cell line, changes in cell cycle progression recorded within 24 h incubation share some similarities (Fig. 8C). First, within the first 12 h, both compounds induced accumulation of cells in the G0/G1 phase. This effect was notably prominent in the samples treated with **1**, accompanied with reduced percentage of cells in both S and G2/M phases. Second, at 12 h incubation both compounds caused accumulation of treated cells in the S phase, which at this point was markedly more intensive in the samples treated with CDDP. Nevertheless, distribution of treated cells at 24 h has finally confirmed the assumption after Annexin-V/PI analysis (Fig. 8A): while cells treated with **1** were still slightly accumulated in the S phase, those subjected to CDDP ended in the G1-to-S block, which clearly defined that those two compounds do not share the same mechanism of activity. Therefore, CDDP at 24 h acts as an anti-proliferative agent rather than a pro-apoptotic one, although it is not be possible to designate if AnnexinV single-stained cells in CDDP-treated samples will end up in apoptosis or necrosis. On the other hand, treatment with **1** easily triggers apoptosis within several hours of incubation, and more important, efficiently drives THP-1 cells through the process of apoptotic death. Current results are opposite to those previously published for CDDP using the same biological models and experimental conditions.[56] The prominent characteristic of CDDP activity is its interstrand cross-linking to DNA. Although interstrand cross-links account for only a few percentages of all CDDP adducts those are the crucial for DNA unwinding, activation of complex repair pathways with cell cycle arrest at the S phase, and finally apoptotic death.[104,105] Those reasons explain the delayed onset of apoptosis in cells treated with CDDP compared to the effect of **1**.[56] The decisive issue that confirms distinction between mechanisms of CDDP and **1** activities is the results of pUC19 electrophoresis, where **1** induced only a retardation of supercoiled form contrary to massively unwound form seen in the presence of CDDP.[106]

Previously, we described the activity of caspases in cells treated with CDDP.[56] Briefly, co-treatment of THP-1 cells with CDDP and pan-caspase inhibitor Z-VAD-fmk revealed that apoptosis induced by CDDP was not exclusively caspase-dependent. Also, treatment of THP-1 cells with CDDP for 6 h did not induce activation of either caspase-8 or caspase-947. When THP-1 cells were co-incubated with Z-VAD-fmk and 1, average of 35 ± 3% of apoptotic events were inhibited compared to the samples treated with 1 only (Fig. 9A). We also calculated percentages of reduced events in early and late phases of apoptotic death and that result undoubtedly revealed that the inhibition of caspases activity primarily prevented initiation of

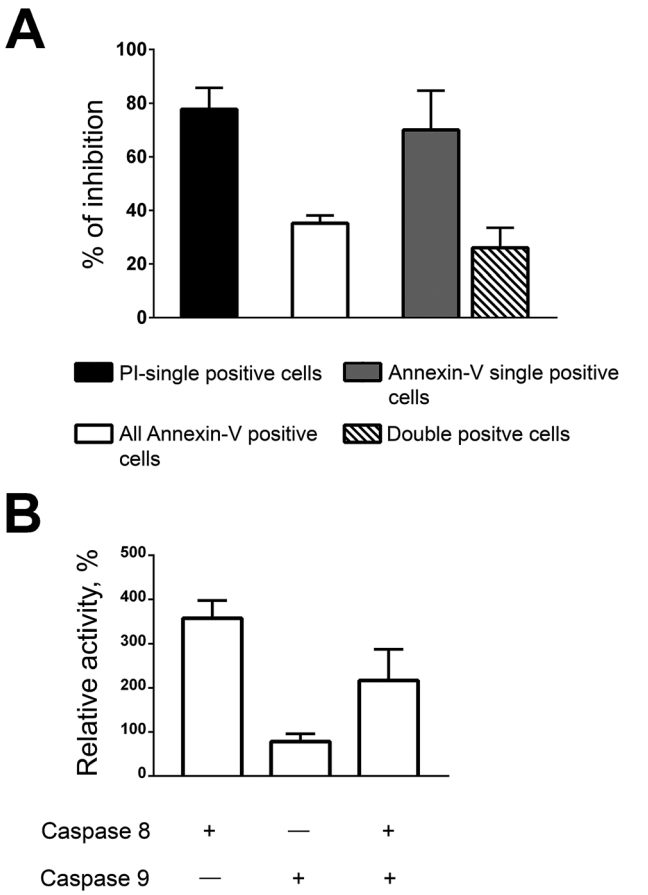

Fig. 9 Role of caspases activation in apoptotic death of THP-1 cells after 6 h treatment with **1** applied at ED_{50} concentration. Percentage of apoptosis inhibition due to co-incubation of treated cells with pan-caspase inhibitor Z-VAD-fmk (A), and relative change of caspase-8 and -9 activity in treated cells computed in regard to non-treated control (B). Both results are expressed as the mean ± SD of two replicated from independent experiments.

apoptotic death in THP-1 cells rather than it hampered its execution (70 ± 14% of early apoptotic events inhibited *vs.* 26 ± 7% late apoptotic events). It is particularly interesting that co-treatment with Z-VAD-fmk did not stimulate incidence of necrotic death that could be expected due to interrupted chain of cascade interactions, quite on the contrary necrosis was also reduced in a high percentage (78 ± 8%). This indicates that cells, withheld from entering apoptosis due to inhibition of caspases activity, do not end in necrosis. This further refers to the mechanism by which **1** triggers apoptotic process, that does not include substantial damage of cellular integrity, but involves an initiation of cascade interactions with caspase activation at the very onset.

Additional evaluation of caspases activity revealed that treatment with **1** induced activation of caspase-8 in THP-1 cells (Fig. 9B). In regard to untreated control, 357 ± 40% of treated cells were expressing activated caspase-8 only, while 78 ± 18% cells were expressing activated caspase-9. Apparently, due to the cross-talk activation between two apoptotic pathways, 217 ± 71% of treated cells displayed activated both caspase-8 and -9. Prevailing activation of caspase-8 demonstrates the **1** triggered apoptotic death either by activation of death receptor signaling cascade[107] or by endoplasmic reticulum stress.[108] This finding additionally supports the difference between mechanisms of CDDP and **1** activity.

When activation of caspase-8 was identified as mechanism responsible for triggering of apoptosis in THP-1 cells treated with **1**, we hesitated to evaluate its activity on AsPC-1 cells since it was previously shown that this cell line is low expressing Fas ligand that might be involved in the initiation of apoptotic death.[109] CDDP did not show significant activity on AsPC-1 cells.[56] Even more, while arrest at the S phase was seen only after treatment with the lowest applied concentration of CDDP that was not accompanied with apoptotic response, percentages of cells at the cell cycle phases in samples treated with higher concentrations barely varied compared to untreated control. As expected, treatment of AsPC-1 cells with **1** did not affect their survival (Fig. 10), however, changes in cell cycle distribution were far more impressive than those induced by CDDP. It is important to notice that these cells are poorly differentiated, referred to as Cancer Stem Cells (CSCs).[110] CSCs, also named as tumor-initiating or tumor-propagating cells, are rare immortal cells within the tumor bulk that possess a number of biological properties that distinguish them from remaining tumor cells, such as resistance to treatment and evasion of cell death by ability to conceal into the state of dormancy,[111] and that was observed in the samples treated with **1**. Contrary to CDDP, **1** evoked accumulation of AsPC-1 cells at the S phase only in the samples treated with **1** and 10 μM, but higher concentrations drove them toward G0/G1 block not accompanied with increase of either apoptotic or necrotic events. While AsPC-1 cells were obviously unaffected by the treatment with CDDP, the same cell line was provoked by **1** and its mechanism of activity, escaping apoptosis by hiding in the state of dormancy, at least for the first 24 h of incubation.

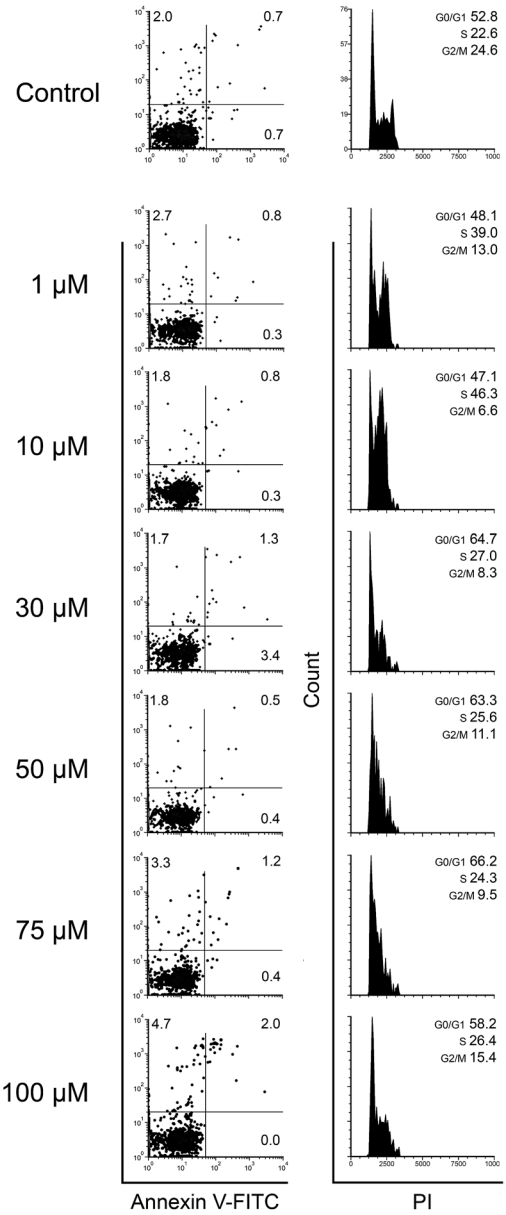

Fig. 10 Types of cell death and cell cycle changes in AsPC-1 cell line induced by the treatment with **1** during 24 h incubation. In Annexin V/PI dot plots (left panel) cells are discriminated as viable (non-stained cells, lower left quadrant), cells in early phase of apoptotic death (Annexin V single-stained cells, lower right quadrant), cells in advanced phases of apoptotic death (double-stained cells, upper right quadrant), and necrotic cells (PI single-stained cells, upper left quadrant). Cell cycle changes (right panel) were determined as percentage of cells at the G0/G1, S and G2/M phases of mitotic division according to non-treated control population. All results are expressed as percentages of one replicate.

Conclusions

Novel nickel(II) square-planar hydrazone complex **1** was synthesized and characterized, and its geometry was optimized by DFT calculations. IR spectroscopy results indicate asymmetrical coordination of ligand's arms, which was also found in

the solution, as evidenced by NMR spectroscopy. Investigation of thermal stability of **1** showed that it is thermally stable at temperatures below 160 °C, while the initial degradation processes in air and nitrogen exhibit relatively high values of overall apparent activation energy of 250–300 and 1150–1200 kJ mol^{-1}, respectively. This property makes the complex suitable for long-term storage at normal ambient temperatures, with easier potential medical and biological usage.

Current investigation provided experimental validation for the ability of **1** to covalently bind to DNA, which is also well-known feature of CDDP. However, the series of our results revealed that the mechanism of anticancer activity for these two compounds is completely different. After 24 h incubation on THP-1 cells **1** induces powerful apoptotic response accompanied with slight accumulation of cells at the S phase of mitotic division. Apoptosis driven by **1** is partially caspase-dependent with dominantly activated caspase-8. Therefore, the results presented here strongly indicate that **1** has a different, more efficient mode of anticancer activity than CDDP. Concentration-dependent shift in the cell cycle distribution of AsPC-1 cells, experimentally confirmed covalent binding to DNA, and activation of caspase-8 strongly indicates that **1** exhibits at least two mechanisms of anticancer activity. The induced caspase-8 activation by **1** sets it as a primary interest in any further investigation.

Acknowledgements

The authors acknowledge networking support by the COST Action CM1106 StemChem – "Chemical Approaches to Targeting Drug Resistance in Cancer Stem Cells". The work was funded by the Ministry of Education, Science and Technological Development of the Republic of Serbia (Grant 172055 and 172057).

References

1 C. F. Wise, D. Liu, K. J. Mayer, P. M. Crossland, C. L. Hartley and W. R. McNamara, *Dalton Trans.*, 2015, **44**, 14265–14271.
2 D. Sadhukhan, A. Ray, G. Pilet, C. Rizzoli, G. M. Rosair, C. J. Gómez-García, S. Signorella, S. Bellú and S. Mitra, *Inorg. Chem.*, 2011, **50**, 8326–8339.
3 C.-S. Tsang, L. Chen, L.-W. Li, S.-M. Yiu, T.-C. Lau and H.-L. Kwong, *Dalton Trans.*, 2015, **44**, 13087–13092.
4 Y. Gao, L. Zhao, X. Xu, G. F. Xu, Y. N. Guo, J. Tang and Z. Liu, *Inorg. Chem.*, 2011, **50**, 1304–1308.
5 Z. Chen, Y. Wu, C. He, B. Wang, D. Gu and F. Gan, *Synth. Met.*, 2010, **160**, 2581–2586.
6 Z. M. Chen, Y. Q. Wu, D. H. Gu and F. X. Gan, *Appl. Phys. A: Mater. Sci. Process.*, 2007, **88**, 409–414.
7 H. Abd El-Wahab, M. Abd El-Fattah, A. H. Ahmed, A. A. Elhenawy and N. A. Alian, *J. Organomet. Chem.*, 2015, **791**, 99–106.
8 H. Küpper and P. M. H. Kroneck, in *Nickel and Its Surprising Impact in Nature: Metal Ions in Life Sciences*, ed. R. K. O. Sigel, A. Sigel and H. Sigel, John Wiley & Sons Ltd, Chichester, 2007, vol. 2, pp. 31–62.
9 S. Oshin and A. Thapa, *J. Chem. Pharm. Res.*, 2015, **7**, 953–963.
10 A. Abu-Surrah and M. Kettunen, *Curr. Med. Chem.*, 2006, **13**, 1337–1357.
11 P. Krishnamoorthy, P. Sathyadevi, R. R. Butorac, A. H. Cowley, N. S. P. Bhuvanesh and N. Dharmaraj, *Dalton Trans.*, 2012, **41**, 6842.
12 H. J. Zhong, L. Lu, K. H. Leung, C. C. L. Wong, C. Peng, S. C. Yan, D. L. Ma, Z. Cai, H. M. D. Wang and C. H. Leung, *Chem. Sci.*, 2015, **6**, 5400–5408.
13 L. J. Liu, L. Lu, H. J. Zhong, B. He, D. W. J. Kwong, D. L. Ma and C. H. Leung, *J. Med. Chem.*, 2015, **58**, 6697–6703.
14 C. Zhao, X. Chen, D. Zang, X. Lan, S. Liao, C. Yang, P. Zhang, J. Wu, X. Li, N. Liu, Y. Liao, H. Huang, X. Shi, L. Jiang, X. Liu, Z. He, Q. P. Dou, X. Wang and J. Liu, *Oncogene*, 2016, 1–12.
15 F. Bisceglie, S. Pinelli, R. Alinovi, M. Goldoni, A. Mutti, A. Camerini, L. Piola, P. Tarasconi and G. Pelosi, *J. Inorg. Biochem.*, 2014, **140**, 111–125.
16 J. Chen, Y. W. Huang, G. Liu, Z. Afrasiabi, E. Sinn, S. Padhye and Y. Ma, *Toxicol. Appl. Pharmacol.*, 2004, **197**, 40–48.
17 S. Datta, D. K. Seth, S. Gangopadhyay, P. Karmakar and S. Bhattacharya, *Inorg. Chim. Acta*, 2012, **392**, 118–130.
18 N. Gligorijević, T. Todorović, S. Radulović, D. Sladić, N. Filipović, D. Godevac, D. Jeremić and K. Andelković, *Eur. J. Med. Chem.*, 2009, **44**, 1623–1629.
19 R. Gomathi, A. Ramu and A. Murugan, *Bioinorg. Chem. Appl.*, 2014, **2014**, 1–12.
20 P. Kalaivani, R. Prabhakaran, F. Dallemer and K. Natarajan, *RSC Adv.*, 2014, **4**, 51850–51864.
21 P. Kalaivani, S. Saranya, P. Poornima, R. Prabhakaran, F. Dallemer, V. Vijaya Padma and K. Natarajan, *Eur. J. Med. Chem.*, 2014, **82**, 584–599.
22 P. Li, M. Niu, M. Hong, S. Cheng and J. Dou, *J. Inorg. Biochem.*, 2014, **137**, 101–108.
23 S. A. Osman, H. A. Mousa, H. A. A. Yosef, T. S. Hafez, A. A. El-Sawy, M. M. Abdallah and A. S. Hassan, *J. Serb. Chem. Soc.*, 2014, **79**, 953–964.
24 R. Prabhakaran, P. Kalaivani, R. Huang, P. Poornima, V. Vijaya Padma, F. Dallemer and K. Natarajan, *J. Biol. Inorg. Chem.*, 2013, **18**, 233–247.
25 R. Prabhakaran, P. Kalaivani, P. Poornima, F. Dallemer, G. Paramaguru, V. Vijaya Padma, R. Renganathan, R. Huang and K. Natarajan, *Dalton Trans.*, 2012, **41**, 9323.
26 E. Ramachandran, D. S. Raja, J. L. Mike, T. R. Wagner, M. Zeller and K. Natarajan, *RSC Adv.*, 2012, **2**, 8515.
27 L. Shi, R.-Q. Fang, J.-Y. Xue, Z.-P. Xiao, S.-H. Tan and H.-L. Zhu, *Aust. J. Chem.*, 2008, **61**, 288.
28 T. A. Yousef, G. M. Abu El-Reash, M. Al-Jahdali and E. B. R. El-Rakhawy, *Spectrochim. Acta, Part A*, 2014, **129**, 163–172.
29 S. Zhang, J. Dong, X. Fan, Y. Chen and J. Zhou, *J. Coord. Chem.*, 2012, **65**, 3098–3110.
30 W. Liu and R. Gust, *Chem. Soc. Rev.*, 2013, **42**, 755–773.

31 P. Battistini, M. Carcelli, E. Dalcanale, C. Pelizzi, G. Pelizzi and L. Righini, *Mol. Cryst. Liq. Cryst. Sci. Technol., Sect. A*, 1998, **309**, 167–188.
32 M. Carcelli, S. Ianelli, L. Mavilla, C. Pelizzi and G. Pelizzi, *Inorg. Chim. Acta*, 1996, **245**, 43–49.
33 N. C. Kasuga, K. Sekino, C. Koumo, N. Shimada, M. Ishikawa and K. Nomiya, *J. Inorg. Biochem.*, 2001, **84**, 55–65.
34 G. Pelizzi, A. Bacchi, I. Ivanovic-Burmazovic, M. Gruden and K. Andjelkovic, *Inorg. Chem. Commun.*, 2001, **4**, 311–314.
35 M. V. Plutenko, Y. S. Moroz, T. Y. Sliva, M. Haukka and I. O. Fritsky, *Acta Crystallogr., Sect. C: Cryst. Struct. Commun.*, 2008, **64**, 137–139.
36 T. R. Todorović, A. Bacchi, G. Pelizzi, N. O. Juranić, D. M. Sladić, I. D. Brčeski and K. K. Andelković, *Inorg. Chem. Commun.*, 2006, **9**, 862–865.
37 R. C. Maia, R. Tesch and C. A. M. Fraga, *Expert Opin. Ther. Pat.*, 2014, **24**, 1161–1170.
38 R. Islam, F. Koizumi, Y. Kodera, K. Inoue, T. Okawara and M. Masutani, *Bioorg. Med. Chem. Lett.*, 2014, **24**, 3802–3806.
39 R. Eshkourfu, B. Čobeljić, M. Vujčić, I. Turel, A. Pevec, K. Sepčić, M. Zec, S. Radulović, T. Srdić-Radić, D. Mitić, K. Andjelković and D. Sladić, *J. Inorg. Biochem.*, 2011, **105**, 1196–1203.
40 M. Vujčić, M. Lazić, M. Milenković, D. Sladić, S. Radulović, N. Filipović and K. Andjelković, *J. Biochem. Mol. Toxicol.*, 2011, **25**, 175–182.
41 N. R. Filipović, A. Bacchi, M. Lazić, G. Pelizzi, S. Radulović, D. M. Sladić, T. R. Todorović and K. K. Andjelković, *Inorg. Chem. Commun.*, 2008, **11**, 47–50.
42 B. Singh and U. R. Singh, *Transition Met. Chem.*, 1995, **20**, 100–103.
43 S. A. M. Metwally, M. I. Abdel Moneim, Y. A. Elossely, R. I. Awad and K. Abou-Hadeed, *Chem. Heterocycl. Compd.*, 2010, **46**, 426–437.
44 V. Blagojević, *ThermV software package*, 2014, https://sourceforge.net/projects/thermv.
45 M. J. Frisch, G. W. Trucks, H. B. Schlegel, G. E. Scuseria, M. A. Robb, J. R. Cheeseman, G. Scalmani, V. Barone, B. Mennucci, G. A. Petersson, H. Nakatsuji, M. Caricato, X. Li, H. P. Hratchian, A. F. Izmaylov, J. Bloino, G. Zheng, J. L. Sonnenberg, M. Hada, M. Ehara, K. Toyota, R. Fukuda, J. Hasegawa, M. Ishida, T. Nakajima, Y. Honda, O. Kitao, H. Nakai, T. Vreven, J. A. Montgomery Jr, J. E. Peralta, F. Ogliaro, M. Bearpark, J. J. Heyd, E. Brothers, K. N. Kudin, V. N. Staroverov, R. Kobayashi, J. Normand, K. Raghavachari, A. Rendell, J. C. Burant, S. S. Iyengar, J. Tomasi, M. Cossi, N. Rega, J. M. Millam, M. Klene, J. E. Knox, J. B. Cross, V. Bakken, C. Adamo, J. Jaramillo, R. Gomperts, R. E. Stratmann, O. Yazyev, A. J. Austin, R. Cammi, C. Pomelli, J. W. Ochterski, R. L. Martin, K. Morokuma, V. G. Zakrzewski, G. A. Voth, P. Salvador, J. J. Dannenberg, S. Dapprich, A. D. Daniels, Ö. Farkas, J. B. Foresman, J. V. Ortiz, J. Cioslowski and D. J. Fox, *Gaussian 09, Revision D.01*, Gaussian Inc., Wallingford, CT, 2009.
46 F. Neese, *Wiley Interdiscip. Rev.: Comput. Mol. Sci.*, 2012, **2**, 73–78.
47 S. Sinnecker, A. Rajendran, A. Klamt, M. Diedenhofen and F. Neese, *J. Phys. Chem. A*, 2006, **110**, 2235–2245.
48 A. D. Becke, *Phys. Rev. A*, 1988, **38**, 3098–3100.
49 C. Lee, W. Yang and R. G. Parr, *Phys. Rev. B: Condens. Matter Mater. Phys.*, 1988, **37**, 785–789.
50 J. P. Perdew, *Phys. Rev. B: Condens. Matter Mater. Phys.*, 1986, **33**, 8822–8824.
51 J. P. Perdew, K. Burke and M. Ernzerhof, *Phys. Rev. Lett.*, 1996, **77**, 3865–3868.
52 J. P. Perdew, K. Burke and M. Ernzerhof, *Phys. Rev. Lett.*, 1997, **78**, 1396.
53 M. H. Jamroz, *Vibrational Energy Distribution Analysis VEDA 4*, Warsaw, 2004–2010.
54 S. Ghosh, P. Kundu, B. K. Paul and N. Chattopadhyay, *RSC Adv.*, 2014, **4**, 63549–63558.
55 J. Sambrook, E. F. Fritsch and T. Maniatis, *Molecular cloning: A laboratory manual*, Cold Spring Harb. Lab. Press, 2nd edn, 1989, p. 626.
56 N. R. Filipović, S. Bjelogrlić, A. Marinković, T. Ž. Verbić, I. N. Cvijetić, M. Senćanski, M. Rodić, M. Vujčić, D. Sladić, Z. Striković, T. R. Todorović and C. D. Muller, *RSC Adv.*, 2015, **5**, 95191–95211.
57 W. J. Geary, *Coord. Chem. Rev.*, 1971, **7**, 81–122.
58 H. E. Gottlieb, V. Kotlyar and A. Nudelman, *J. Org. Chem.*, 1997, **62**, 7512–7515.
59 I. M. Angulo, E. Bouwman, S. M. Lok, M. Lutz, W. P. Mul and A. L. Spek, *Eur. J. Inorg. Chem.*, 2001, 1465–1473.
60 G. R. Fulmer, A. J. M. Miller, N. H. Sherden, H. E. Gottlieb, A. Nudelman, B. M. Stoltz, J. E. Bercaw and K. I. Goldberg, *Organometallics*, 2010, **29**(9), 2176–2179.
61 S. Yoo, J. Kum and S. Cho, *Nanoscale Res. Lett.*, 2011, **6**, 545.
62 L. Leonat, G. Sbarcea and I. V. Branzoi, *UPB Scientific Bulletin, Series B: Chemistry and Materials Science*, 2013, **75**, 111–118.
63 J. L. Bredas, R. Silbey, D. S. Boudreaux and R. R. Chance, *J. Am. Chem. Soc.*, 1983, **105**, 6555–6559.
64 H. E. Kissinger, *Anal. Chem.*, 1957, **29**, 1702–1706.
65 T. J. Ozawa, *J. Therm. Anal.*, 1970, **2**, 301–324.
66 B. J. Pages, D. L. Ang, E. P. Wright and J. R. Aldrich-Wright, *Dalton Trans.*, 2015, **44**, 3505–3526.
67 J. Ruiz, C. Vicente, C. de Haro and D. Bautista, *Inorg. Chem.*, 2013, **52**, 974–982.
68 J. Ruiz, V. Rodríguez, N. Cutillas, K. G. Samper, M. Capdevila, Ò. Palacios and A. Espinosa, *Dalton Trans.*, 2012, **41**, 12847.
69 N. C. Garbett, N. B. Hammond and D. E. Graves, *Biophys. J.*, 2004, **87**, 3974–3981.
70 F. Dimiza, S. Fountoulaki, A. N. Papadopoulos, C. A. Kontogiorgis, V. Tangoulis, C. P. Raptopoulou, V. Psycharis, A. Terzis, D. P. Kessissoglou and G. Psomas, *Dalton Trans.*, 2011, **40**, 8555.
71 E. S. Koumousi, M. Zampakou, C. P. Raptopoulou, V. Psycharis, C. M. Beavers, S. J. Teat, G. Psomas and T. C. Stamatatos, *Inorg. Chem.*, 2012, **51**, 7699–7710.

72 S. Mardanya, S. Karmakar, D. Maity and S. Baitalik, *Inorg. Chem.*, 2015, **54**, 513–526.
73 X. Ling, W. Zhong, Q. Huang and K. Ni, *J. Photochem. Photobiol., B*, 2008, **93**, 172–176.
74 Z. Moradi, M. Khorasani-Motlagh and M. Noroozifar, *J. Biomol. Struct. Dyn.*, 2016, **1102**, 1–12.
75 H.-L. Wu, W.-Y. Li, X.-W. He, K. Miao and H. Liang, *Anal. Bioanal. Chem.*, 2002, **373**, 163–168.
76 W. Y. Lee, Y. K. Yan, P. P. F. Lee, S. J. Tan and K. H. Lim, *Metallomics*, 2012, **4**, 188–196.
77 N. Mahalakshmi and R. Rajavel, *Arabian J. Chem.*, 2014, **7**, 509–517.
78 P. Tamil Selvi, H. Stoeckli-Evans and M. Palaniandavar, *J. Inorg. Biochem.*, 2005, **99**, 2110–2118.
79 C. Rajarajeswari, R. Loganathan, M. Palaniandavar, E. Suresh, A. Riyasdeen and M. A. Akbarsha, *Dalton Trans.*, 2013, **42**, 8347.
80 C. Icsel and V. T. Yilmaz, *J. Photochem. Photobiol., B*, 2014, **130**, 115–121.
81 M.-J. Li, T.-Y. Lan, X.-H. Cao, H.-H. Yang, Y. Shi, C. Yi and G.-N. Chen, *Dalton Trans.*, 2014, **43**, 2789–2798.
82 S. S. Mati, S. S. Roy, S. Chall, S. Bhattacharya and S. C. Bhattacharya, *J. Phys. Chem. B*, 2013, **117**, 14655–14665.
83 T. Sarwar, S. U. Rehman, M. A. Husain, H. M. Ishqi and M. Tabish, *Int. J. Biol. Macromol.*, 2015, **73**, 9–16.
84 X. Zhou, G. Zhang and J. Pan, *Int. J. Biol. Macromol.*, 2015, **74**, 185–194.
85 B. Mavroidi, M. Sagnou, K. Stamatakis, M. Paravatou-Petsotas, M. Pelecanou and C. Methenitis, *Inorg. Chim. Acta*, 2016, **444**, 63–75.
86 C. Polonyi, I. Albertsson, M. S. Damian and S. K. C. Elmroth, *Zeitschrift für Anorg. und Allg. Chemie*, 2013, **639**, 1655–1660.
87 E. Robles-Escajeda, A. Martínez, A. Varela-Ramirez, R. A. Sánchez-Delgado and R. J. Aguilera, *Cell Biol. Toxicol.*, 2013, **29**, 431–443.
88 V. Cepeda, M. Fuertes, J. Castilla, C. Alonso, C. Quevedo and J. Perez, *Anti-Cancer Agents Med. Chem.*, 2007, **7**, 3–18.
89 N. Grover, T. W. Welch, T. A. Fairley, M. Cory and H. H. Thorp, *Inorg. Chem.*, 1994, **33**, 3544–3548.
90 Z. Chen, X. Wang, Y. Zhu, Y. Li and Z. Guo, *J. Inorg. Biochem.*, 2007, **101**, 1894–1902.
91 N. Abrescia, *Nucleic Acids Res.*, 1999, **27**, 1593–1599.
92 H. Sigel, S. S. Massoud and N. A. Corfu, *J. Am. Chem. Soc.*, 1994, **116**, 2958–2971.
93 S. L. H. Higgins, T. A. White, B. S. J. Winkel and K. J. Brewer, *Inorg. Chem.*, 2011, **50**, 463–470.
94 M. Milkevitch, H. Storrie, E. Brauns, K. J. Brewer and B. W. Shirley, *Inorg. Chem.*, 1997, **36**, 4534–4538.
95 S. Swavey, M. DeBeer and K. Li, *Inorg. Chem.*, 2015, **54**, 3139–3147.
96 D. K. Treiber, X. Zhai, H. M. Jantzen and J. M. Essigmann, *Proc. Natl. Acad. Sci. U. S. A.*, 1994, **91**, 5672–5676.
97 A. Brozovic, A. Ambriović-Ristov and M. Osmak, *Crit. Rev. Toxicol.*, 2010, **40**, 347–359.
98 B. Desoize, *Critical Reviews in Oncology/Hematology*, 2002, **42**, 1–3.
99 D. Wang and S. J. Lippard, *J. Biol. Chem.*, 2004, **279**, 20622–20625.
100 S.-Y. Xie, Y.-J. Li, P.-Y. Wang, F. Jiao, S. Zhang and W.-J. Zhang, *Oncol. Rep.*, 2010, **23**, 1693–1700.
101 A.-M. Florea and D. Büsselberg, *BioMetals*, 2006, **19**, 419–427.
102 F. Splettstoesser, A.-M. Florea and D. Büsselberg, *Br. J. Pharmacol.*, 2009, **151**, 1176–1186.
103 A. Tomaszewski and D. Büsselberg, *Neurotoxicology*, 2007, **28**, 49–58.
104 J.-M. Malinge, M.-J. Giraud-Panis and M. Leng, *J. Inorg. Biochem.*, 1999, **77**, 23–29.
105 J. M. Wagner and L. M. Karnitz, *Mol. Pharmacol.*, 2009, **76**, 208–214.
106 M. V. Keck and S. J. Lippard, *J. Am. Chem. Soc.*, 1992, **114**, 3386–3390.
107 Z. Mahmood and Y. Shukla, *Exp. Cell Res.*, 2010, **316**, 887–899.
108 A. Jimbo, E. Fujita, Y. Kouroku, J. Ohnishi, N. Inohara, K. Kuida, K. Sakamaki, S. Yonehara and T. Momoi, *Exp. Cell Res.*, 2003, **283**, 156–166.
109 K. Yuan, G. Jing, J. Chen, H. Liu, K. Zhang, Y. Li, H. Wu, J. M. McDonald and Y. Chen, *J. Biol. Chem.*, 2011, **286**, 24776–24784.
110 B. Beck and C. Blanpain, *Nat. Rev. Cancer*, 2013, **13**, 727–738.
111 A. Kreso and J. E. Dick, *Cell Stem Cell*, 2014, **14**, 275–291.